

What are the Radial Distributions of Density, Outflow Rates, and Cloud Structures in the M 82 Wind?

XINFENG XU,¹ TIMOTHY HECKMAN,¹ MICHITOSHI YOSHIDA,² ALAINA HENRY,^{1,3} AND YOUICHI OHYAMA⁴

¹Center for Astrophysical Sciences, Department of Physics & Astronomy, Johns Hopkins University, Baltimore, MD 21218, USA

²National Astronomical Observatory of Japan, Osawa, Mitaka, Tokyo 181-8588, Japan

³Space Telescope Science Institute, 3700 San Martin Drive, Baltimore, MD 21218, USA

⁴Institute of Astronomy and Astrophysics, Academia Sinica, 11F of Astronomy-Mathematics Building, No.1, Sec. 4, Roosevelt Rd, Taipei 10617, Taiwan, R.O.C.

Submitted to AASJournal ApJ

ABSTRACT

Galactic winds play essential roles in the evolution of galaxies through the feedback they provide. Despite intensive studies of winds, the radial distributions of their properties and feedback are rarely observable. Here we present such measurements for the prototypical starburst galaxy, M 82, based on observations by Subaru telescope. We determine the radial distribution of outflow densities (n_e) from the spatially-resolved [S II] $\lambda\lambda 6717, 6731$ emission-lines. We find n_e drops from 200 to 40 cm^{-3} with radius (r) between 0.5 and 2.2 kpc with a best-fit power-law index of $r^{-1.2}$. Combined with resolved H α lines, we derive mass, momentum, and energy outflow rates, which drop quite slowly (almost unchanged within error bars) over this range of r . This suggests that the galactic wind in M 82 can carry mass, momentum, and energy from the central regions to a few kpc with minimal losses. We further derive outflow cloud properties, including size and column densities. The clouds we measure have pressures and densities that are too high to match those from recent theoretical models and numerical simulations of winds. By comparing with a sample of outflows in local star-forming galaxies studied with UV absorption-lines, the above-derived properties for M 82 outflows match well with the published scaling relationships. These matches suggest that the ionized gas clouds traced in emission and absorption are strongly related. Our measurements motivate future spatially resolved studies of galactic winds, which is the only way to map the structure of their feedback effects.

Keywords: Galactic Winds (572), Galaxy evolution (1052), Galaxy kinematics and dynamics(602), Starburst galaxies (1570), Galaxy spectroscopy (2171)

1. INTRODUCTION

Galactic winds, which are driven by energy and momentum supplied by star-formation (SF) or active galactic nuclei (AGNs), play an essential role in the evolution of galaxies (e.g., Chevalier & Clegg 1985; Silk & Rees 1998). They are responsible for various feedback effects, including regulating SF in galaxies, enriching the intergalactic and circumgalactic medium (IGM and CGM) with metals, and reducing the baryons in galactic discs to solve the “overcooling problem” (see reviews in Naab & Ostriker 2017; Donahue & Voit 2022; Heckman & Best 2023; and references therein).

The current understanding of starburst-driven galactic winds is that the energy source is provided by stellar winds and core-collapse supernovae from the population of massive stars (Chevalier & Clegg 1985). These ejecta are thermalized in shocks to produce a very hot (up to $\sim 10^8$ K) fluid which expands outward to form a very fast (up to 3000 km/s) and tenuous wind. This wind fluid interacts with ambient gas clouds, accelerating them outward at velocities of 10^2 to 10^3 km/s. These outflowing clouds span a wide range of phases, including hot (few million K), warm ionized (10^4 K), neutral atomic, and molecular gas (e.g., Leroy et al. 2015). These outflowing clouds can be readily observed in both emission and absorption (see reviews in Heckman & Thompson 2017; Veilleux et al. 2020).

Constraining the impact of galactic winds requires estimating the total mass/energy/momentum that outflows carry. In

principle, these can be measured for the different gas phases listed above. These quantities are commonly characterized as outflow rates, i.e., mass/energy/momentum carried by the outflowing material per unit time. In SF galaxies, which are the focus of this paper, the most extensive such studies refer to the warm ionized gas, from UV and optical absorption lines (e.g., Heckman et al. 2000; Pettini et al. 2000; Rupke et al. 2002; Martin 2005; 2006; Grimes et al. 2009; Weiner et al. 2009; Rubin et al. 2010; Steidel et al. 2010; Martin et al. 2012; Bordoloi et al. 2014; Rubin et al. 2014; Heckman et al. 2015; Heckman & Borthakur 2016; Chisholm et al. 2016a;b; 2017; Sugahara et al. 2017; Chisholm et al. 2018; Wang et al. 2022; Xu et al. 2022), and from optical emission lines (e.g., Heckman et al. 1990; Lehnert & Heckman 1996; Newman et al. 2012a;b; Rupke & Veilleux 2013; Wood et al. 2015; Davies et al. 2019; Freeman et al. 2019; Perna et al. 2019; Rupke et al. 2019; Swinbank et al. 2019; Burchett et al. 2021; Zabl et al. 2021; Avery et al. 2022; Marasco et al. 2022).

Nearly all of these previous studies only derived the global outflow rates integrated over the observing aperture, except in a few cases (e.g., Leroy et al. 2015; Burchett et al. 2021). This is mainly due to the lack of spatially-resolved observations of well-extended outflows in nearby galaxies. Nonetheless, it has been long recognized that outflows in SF galaxies are the collections of gas with a large range of radius, velocity, and gas phase (e.g., Heckman & Thompson 2017; Veilleux et al. 2020). Thus, it is critical to map out the wind properties and outflow rates.

Furthermore, the radial distribution of the structures of the outflowing clouds, including their volume filling factors (FF), densities, column densities ($N_{\text{H,cl}}$), and sizes (R_{cl}) are largely unknown (but see Xu et al. 2023). However, these parameters are not only essential in quantifying feedback effects, but also vital to constraining sub-grid physics in theoretical models and numerical simulations of winds. For the latter, recent studies show that the R_{cl} and M_{cl} are the key parameters to determine if outflowing clouds can survive long enough to be accelerated by the hot wind fluid (e.g., Gronke & Oh 2020; Li et al. 2020; Sparre et al. 2020; Fielding & Bryan 2022). However, there currently exist no constraints on the radial distribution of these parameters from observations.

In this paper, we seek to shed light on the radial distribution of outflow rates and cloud properties based on the wealth data on M 82, which is the most intensively studied nearby starburst galaxy. M 82 hosts the best-observed wind in any galaxy, exhibiting clear biconical outflowing multi-phase gas out to distances of at least a few kpc. Detailed studies of the starburst activity and the multi-phase wind are made possible by its proximity (distance ~ 3.89 Mpc, Sakai & Madore 1999), and are summarized in Heckman & Thompson (2017). Combining archival results with new

Subaru imaging and resolved spectroscopic data, we aim to tackle various key problems that have not been well-studied previously:

1. What are the radial distributions of the mass, momentum, and energy outflow rates? Do the distributions imply that winds can supply sufficient mass, momentum, and energy onto scales large enough to impact the CGM?
2. What are the properties of outflowing clouds at different radii? Are they consistent with the cloud-survival criteria in current theoretical models and numerical simulations?
3. How are outflow rates connected between different phases? What are the overall combined feedback effects of these phases?

The structure of this paper is as follows. In Section 2, we introduce the observations and data. Then we describe how to calculate outflow density, rates, and cloud properties in Section 3, where we also present the radial profiles of these derived parameters. In Section 4, we discuss and compare our results with measurements of outflow rates estimated for other gas phases. We also place the M 82 outflow in the context of a large sample of local SF galaxies and compare our results to theoretical models and numerical simulations. We conclude the paper in Section 5. Throughout the paper, we adopt a distance to M 82 of 3.89 Mpc (Sakai & Madore 1999), which leads to $18.9 \text{ pc}''$.

2. OBSERVATIONS AND DATA

2.1. Imaging Data

Optical imaging observations of M 82 were conducted with Faint Object Camera And Spectrograph (FOCAS, Kashikawa et al. 2002) on the Subaru Telescope (Kaifu et al. 2000) on February 2000. These images are published in Ohyama et al. (2002). Two narrow-band filters are used, including the N658 filter that has covered the emission lines of $\text{H}\alpha$ $\lambda 6563$ and $[\text{N II}]$ $\lambda\lambda 6548, 6583$; and the N642 filter to detect the adjacent continuum level. Their total exposure times are 600s and 360s, respectively, split into 120s sub-exposures to avoid saturation. The seeing was $0.7''$ to $0.8''$ during the observations. The data were reduced by pipelines in IDL and IRAF (Yoshida et al. 2000). In this paper, we are interested in the $\text{H}\alpha$ emission lines. Thus, we subtract the scaled N642 image from the N658 image to get a pure $\text{H}\alpha$ + $[\text{N II}]$ emission-line map following the same methodology in Ohyama et al. (2002). The result is shown in Figure 1.

2.2. Spectroscopic Data

M 82 was then observed by FOCAS with the spectropolarimetric mode on January 2013. The detailed observations

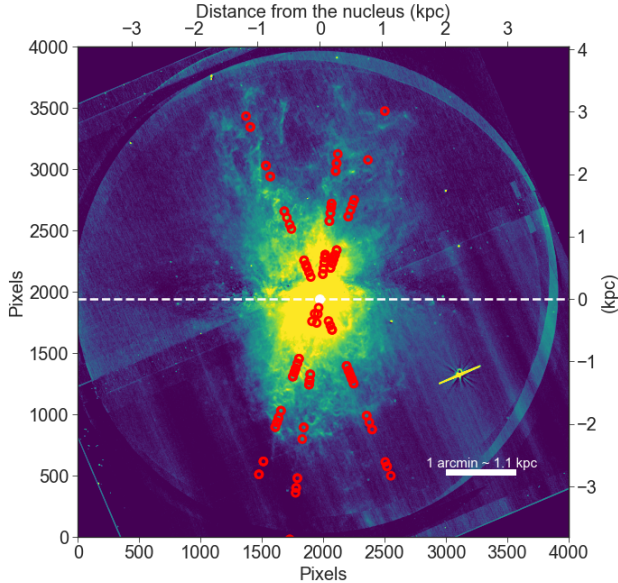


Figure 1. Subaru/FOCAS image of $H\alpha$ + $[N II]$ emission lines (with continuum already subtracted, see Section 2.1). The galaxy disk (white dashed line) has been rotated to be parallel with the x-axis, so the bipolar galactic outflow is perpendicular to the galactic disk (north-west side is up). We overlay the position of FOCAS spectroscopic observations described in Yoshida et al. (2019) as red circles (Section 2.2).

and data reductions are presented in Yoshida et al. (2019). For a summary, the observations adopt a slit mask of eight $0.8'' \times 20.6''$ slitlets at $23.7''$ intervals and a VPH grism with $665 \text{ grooves mm}^{-1}$. These result in a spectral resolution of $R \sim 1700$ and a central wavelength of 6500 \AA , which covered the important emission lines for our analyses, including $H\alpha$ and $[S II] \lambda\lambda 6717, 6731$ doublet. The slits are spatially distributed in three position angles (PAs) and at $\sim 0 - 3 \text{ kpc}$ from the nucleus. We draw the slit locations as the red circles in Figure 1. The total science exposure times are 24,000s. The data were reduced using standard CCD reduction pipelines in IRAF in Yoshida et al. (2019).

3. ANALYSIS AND RESULTS

We start with measuring the radial distributions of the outflow’s electron density and width in Sections 3.1 and 3.2, respectively. These values are then used to calculate the radial distribution of outflow rates in Section 3.3. In Yoshida et al. (2019) the emission-lines are separated into two components given their spectropolarimetric observations: a polarized component due to scattering of the emission from the central starburst by dust in the outflow, and the total light, which is dominated by the intrinsic emission from the outflowing ionized gas. In this paper, we only use the latter.

Since our main tracers are $H\alpha$ and $[S II]$, our calculations in this paper only represent the properties of the warm-ionized phase of outflows ($T \sim 10^4 \text{ K}$). As described in previous publications for M 82 (e.g., Strickland & Heckman 2007; 2009), this warm phase is presumably immersed in and interacting with a dilute volume-filling hot wind fluid ($T \sim \text{few} \times 10^7 - 10^8 \text{ K}$). Hereafter, we distinguish these two components by referring to the former as (warm) outflows, while the latter as (hot) winds.

3.1. Radial Distribution of Outflow Densities

Yoshida et al. (2019) have already derived the electron density (n_e) from the intensity ratio of $[S II] \lambda 6731/\lambda 6717$ for each slit location, assuming a typical ionized gas temperature of 10^4 K (Osterbrock & Ferland 2006). These measurements represent a luminosity-weighted mean density at certain radius. However, these values show moderate scatter (due to intrinsic variations or low S/N) and also contain upper limits (see the gray symbols in Figure 2). Thus, to account for the scatters, we bin their values to get robust estimates of n_e at different radial distances to the galactic center (i.e., r) as follows. We first split the measurements into radial bins given $r_{min} = 0.5 \text{ kpc}$, $r_{max} = 2.5 \text{ kpc}$, and $\log(\Delta r) = 0.1 \text{ dex}$. The cut of r_{min} is because the central region of M 82 is dominated by starburst and does not show clear features of outflows (Shoppell & Bland-Hawthorn 1998; Westmoquette et al. 2013). The cut of r_{max} is due to fewer reliable measurements at larger r reported in Yoshida et al. (2019). This is because the $[S II]$ -based density measurement reaches its low-density limit at $n_e \sim 10 \text{ cm}^{-3}$ (Osterbrock & Ferland 2006), so direct measurements of n_e at larger radii (with lower densities) are not possible. Thus, we adopt survival analysis (which incorporates these upper limits¹) to calculate the average n_e in each radial bin. The results are shown as the red curve in Figure 2. We find that n_e declines from $\sim 200 \text{ cm}^{-3}$ at $r = 0.5 \text{ kpc}$ to $\sim 40 \text{ cm}^{-3}$ at $r = 2.2 \text{ kpc}$. We have fit the data to a power-law and find that $n_e(r) = 100 \times (\frac{r}{1165pc})^{-1.17} \text{ cm}^{-3}$ (see the blue dashed line in Figure 2).

3.2. Radial Distribution of the Lateral Outflow Widths

As shown in Figure 1, the galactic wind exhibits a bipolar structure in $H\alpha$, which is roughly perpendicular to the galaxy disk (rotated to be the x-axis, white dashed line). To better quantify the regions occupied by the $H\alpha$ outflows, we estimate the lateral width of the outflow (W_{out}) at different radial scales as follows.

To remove the background, we first calculate the average counts in blank regions of the image and subtract them from the entire image. Then, for each of the radial bins adopted

¹ We use the *survfit* package in R-language (R Core Team 2021)

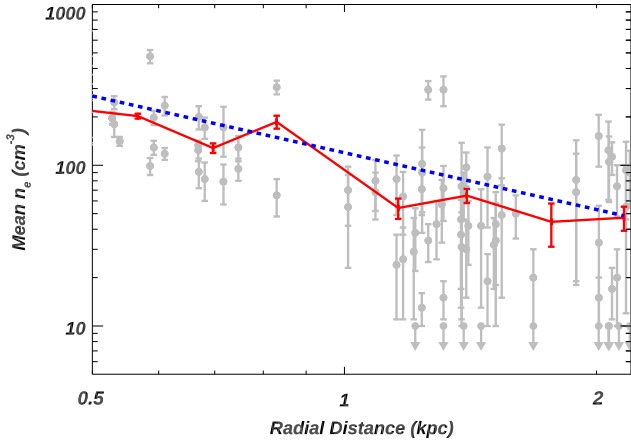


Figure 2. Radial Distribution of electron number density (n_e) for M 82's galactic outflows. The gray symbols are the measurements from [S II] doublet reported in Yoshida et al. (2019) at different slit positions (Figure 1). Their upper limits are shown as arrows. The red curve is the binned n_e at different radii considering the gray data points. We have adopted survival analyses to include the upper limits. We also show the best-fit power-law as the blue dashed line. See section 3.1).

in 3.1, we draw the cumulative $H\alpha$ counts (F_{cum}) as a function of increasing x . An example is shown in the left panel of Figure 3. We then define the lateral width of the $H\alpha$ outflow (i.e., $W_{\text{out}}(H\alpha)$) as the region between $F_{\text{cum}} = 10\%$ and $F_{\text{cum}} = 90\%$. The resulting radial distribution of $W_{\text{out}}(H\alpha)$ is shown in the right panel. We find that $W_{\text{out}}(H\alpha) \sim 1.5 \times r$. If we assume the $H\alpha$ outflow structure is cone-like, this corresponds to an opening angle of 73.7° or a solid angle of 0.4π ster (per cone).

3.3. Radial Distribution of Outflow Rates

To estimate the amounts of mass/energy/momentum carried by the warm ionized outflows per unit time, we can calculate various outflow rates. From the definition, we have:

$$\begin{aligned} \dot{M}_{\text{out}}(r) &= \frac{dM}{dt} = \frac{dM}{dr} \cdot \frac{dr}{dt} = \frac{dM}{dr} V_{\text{out}}(r) \\ \dot{E}_{\text{out}}(r) &= \frac{1}{2} \times \dot{M}_{\text{out}}(r) \times V_{\text{out}}^2(r) \\ \dot{P}_{\text{out}}(r) &= \dot{M}_{\text{out}}(r) \times V_{\text{out}}(r) \end{aligned} \quad (1)$$

where \dot{M}_{out} , \dot{E}_{out} , and \dot{P}_{out} are the mass, energy, and momentum rates of outflows for a certain radial bin, respectively; M and $V_{\text{out}}(r)$ are the mass and velocity of the outflows at this bin, respectively.

For V_{out} , we first adopt the observed line-of-sight (LOS) outflow velocities (V_{obs}) from Shopbell & Bland-Hawthorn (1998), where the measurements are based on detailed maps

of $H\alpha$ emission lines in the southern side of the galaxy². We note the deprojected outflow velocity depends on the orientation of the galaxy and outflows, i.e., $V_{\text{out}} = \text{DF} \times V_{\text{obs}}$, where V_{out} is the deprojected outflow velocity in the rest-frame of M 82 and DF is the deprojection factor. Based on the radial velocity profiles of the double-peaked $H\alpha$ emission mapped over the entire outflow, Shopbell & Bland-Hawthorn (1998) found the best model to fit the data has the geometry as a pair of cones arranged as funnels with $\text{DF} \sim 2$ (see their Section 4.3.4). We adopt their DF hereafter in this paper.

Then we can calculate the volume of a partial cone for a certain radial bin with r_{min} and r_{max} as the lower and upper radii by:

$$\begin{aligned} dVol &= \frac{1}{3} \pi dr \left(\left(\frac{W_{\text{min}}}{2} \right)^2 + \frac{W_{\text{min}} W_{\text{max}}}{2} + \left(\frac{W_{\text{max}}}{2} \right)^2 \right) \\ &= \frac{3}{16} \pi dr \times (r_{\text{min}}^2 + r_{\text{min}} r_{\text{max}} + r_{\text{max}}^2) \end{aligned} \quad (2)$$

In step 2 above, we have adopted $W = 1.5r$ as we measured from $H\alpha$ outflows in Section 3.2. Then we can calculate dM/dr for each radial bin:

$$\frac{dM}{dr} = \frac{dVol}{dr} \times \text{FF} n_e \mu_e \quad (3)$$

where μ_e is the average atomic mass per electron, and FF is the volume filling factor of $H\alpha$ emitting outflows for this bin.

Given n_e has been derived for each radial bin in Section 3.1, the only unknown here is FF. We calculate FF from the $H\alpha$ profiles as:

$$\text{FF} = \frac{F(H\alpha)}{n_e n_p W \times \alpha_{H\alpha} E_{H\alpha}} \quad (4)$$

where $F(H\alpha)$ is the average surface-brightness of $H\alpha$ for a certain radial bin, n_p is the proton number density and we assume $n_p = n_e/1.1$ for fully ionized gas, $\alpha_{H\alpha} = 7.88 \times 10^{-14} \text{ cm}^3 \text{ s}^{-1}$ is the recombination coefficient of $H\alpha$ assuming $T = 10,000 \text{ K}$ (Draine 2011), and $E_{H\alpha} = 3.0 \times 10^{-12} \text{ ergs}$ is the $H\alpha$ photon energy. For $F(H\alpha)$, we measure it from the surface brightness of $H\alpha$ given Subaru/FOCAS spectra (Yoshida et al. 2019) and correct it by the dust extinction measured from Balmer decrements (Heckman et al. 1990). As noted above, due to the higher/uncertain dust extinction on the north-west side, we only compute a dust-corrected $H\alpha$ surface brightness for the south-east side of the outflows. We will finally multiply the resulting outflow rates by a factor of two to represent the total amounts for M 82 (see below).

² The northern side of M 82 is receding from us and is more dusty due to the obscuration by the disk itself. Therefore, measurements of V_{out} and other related parameters are more reliable in southern outflow of M 82 (e.g., Contursi et al. 2013), which is our focus in this paper.

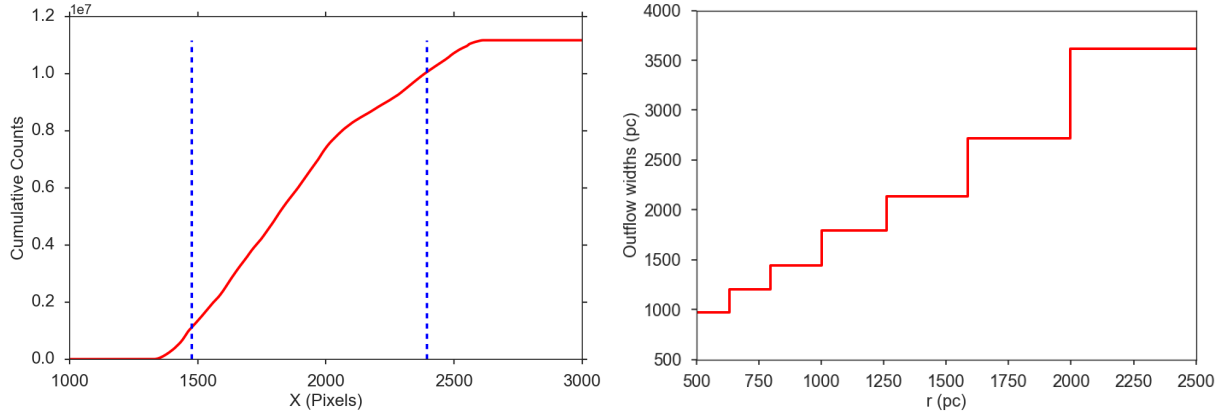


Figure 3. Left: The cumulative counts of H α from Subaru FOCAS image (see Figure 1 and Section 3.2). The two blue dashed lines represent the locations where the cumulative counts equal 10% and 90% of the total counts, separately. We define the outflow width as the region between the blue dashed lines, which is 1.8 kpc for this radial bin. **Right:** Outflow width distribution among different radial distances to the galactic center of M 82 (r).

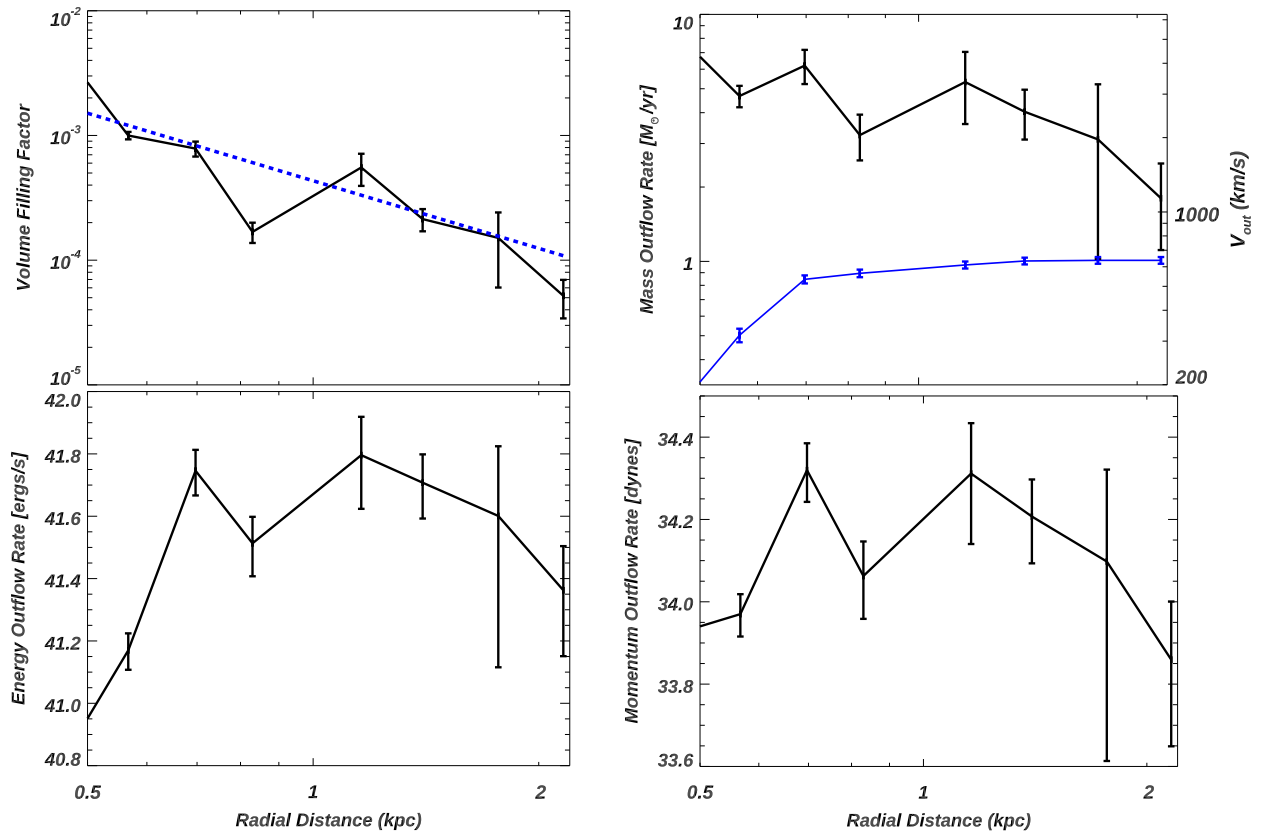


Figure 4. Top-Left: Radial distribution of the volume filling factor (FF) derived from the H α and [S II] emission lines. The best-fit power-law is shown as the blue dashed line. **Top-Right:** The black line represents the radial distribution of mass outflow rates (\dot{M}_{out}) derived in Section 3.3. The blue line represents the de-projected outflow velocity (V_{out}) from H α (Shopbell & Bland-Hawthorn 1998). **Bottom:** Kinetic energy and momentum outflow rates derived in Section 3.3.

The resulting radial distribution of FF is shown in the first panel of Figure 4. We find that FF steadily decreases from 0.3% at $r = 0.5$ kpc to 0.005% at 2.2 kpc, which shows that the warm ionized clouds are extremely clumpy, and occupy less volume as they travel further out of the galaxy. The best-fit power-law is given by $\text{FF}(r) = 10^{-3} \times (\frac{r}{0.288\text{pc}})^{-1.8}$ and is shown as the blue dashed line in Figure 4.

Overall, combining Equations (1) – (4), we can get the radial distributions of \dot{M}_{out} , \dot{E}_{out} , and \dot{P}_{out} for the warm-ionized outflows in M 82 (Figure 4). We find the outflow rates drop quite slowly and stay almost unchanged within the error bars from 0.8 to 2.2 kpc. This suggests that the galactic wind in M 82 can indeed carry the mass, energy, and momentum from the central regions out to a few kpc with minimal losses.

4. DISCUSSION

4.1. Comparisons of Spatially-resolved Multi-phase Outflow Rates in M 82

Detailed spatially-resolved studies of the M 82 wind exist for various outflowing phases. Here we will compare our measured outflow rates as a function of radius from H α and [S II] to the published values for these other phases. Specifically, we will compare to maps of the outflow rates of cold atomic gas (Martini et al. 2018) and cold molecular gas (Leroy et al. 2015). Estimating these rates requires a measurement of the intrinsic outflow velocity. Given the nearly edge-on orientation of M 82, there is a significant correction needed to convert observed line-of-sight outflow velocities to intrinsic values. To be able to compare the outflow rates in the different phases in a consistent way, we use the deprojection factor (DF) adopted for the warm ionized gas to measure outflow rates in the previous studies, i.e., $\text{DF} = 2$ (Shopbell & Bland-Hawthorn 1998; see Section 3.3 above). We have updated their measured outflow rates accordingly. We list the results in Table 1 and briefly discuss these values as follows.

Spatially-resolved maps of the cold neutral outflowing gas in M 82 via spatially resolved H I 21 cm emission were discussed by Martini et al. (2018). Adopting $\text{DF} = 2$, the outflow velocities decline with radius from about 200 km s^{-1} at 1 kpc to only 50 km s^{-1} at 10 kpc. There is a corresponding steep decline in the mass outflow rates. Over the radial range we probe for the warm ionized gas (out to 2.2 kpc), the mass outflow rates in HI are similar to those for the warm ionized gas, but the outflow rates of momentum and (especially) kinetic energy are significantly smaller (Table 1).

Maps of outflowing cold molecular gas in M 82 based on observations of CO emission lines were described by Leroy et al. (2015). For $\text{DF} = 2$, the inferred V_{out} is about 150 km s^{-1} , which is significantly smaller than the values in the warm ionized phase, but similar to the values for the atomic phase. (Table 1). The implied mass outflow rates decline from about $10 M_{\odot} \text{ yr}^{-1}$ at a radius of 1 kpc to values over an order-of-

magnitude smaller by a radius of 3 kpc. Comparing these to the the outflow rates for the warm ionized gas over the the radial range we probe, the mass outflow rates probed by CO are two times larger, the momentum outflow rates are about three times smaller, and the kinetic energy outflow rates are about ten times smaller.

Taken together, the relatively small outflow velocities and the steep decline in outflow rates with radius are consistent with a picture in which the atomic and molecular gas traces a fountain flow that launches gas out to a few kpc (Leroy et al. 2015). We also note that the combined outflow rates of the three phases amount to about 50% of the momentum injected by the M 82 starburst, and only about 16% of the injected kinetic energy. These results are consistent with the finding that the very hot gas ($3 - 8 \times 10^7 \text{ K}$) in M 82 that is feeding the fast wind fluid carries the rest of the momentum flux and nearly all the kinetic energy flux (Strickland & Heckman 2009).

4.2. Comparisons of the Outflow in M 82 to those in the CLASSY Sample

The systematic properties of warm ionized outflows have been widely studied via interstellar absorption lines (e.g., Martin 2005; Rupke et al. 2005; Chisholm et al. 2015; Heckman et al. 2015; Heckman & Borthakur 2016; Xu et al. 2022). However, how the galactic outflow in M 82 as traced in emission compares to these estimates for a large sample of starburst galaxies is still an open question. Here we compare the ionized outflow properties in M 82 with the outflows observed in the COS Legacy Archive Spectroscopy SurveY (CLASSY) atlas (Berg et al. 2022; James et al. 2022). CLASSY includes 45 low-redshift starburst galaxies ($z = 0.002 - 0.182$), which occupy a wide range of important galaxy properties, including stellar mass, SFR, and metallicity. Their outflow features and correlations with the galaxy properties have been analyzed in a homogeneous way and are reported in Xu et al. (2022) and Xu et al. (2023). These results are based on spatially unresolved FUV spectra from the Hubble Space Telescope (HST)/Cosmic Origins Spectrograph (COS).

In Figure 5, we show the outflow velocity versus two important galaxy properties, i.e., stellar mass (left) and SFR (right). The measurements of warm ionized outflows (Section 3) in M 82 are shown as red stars, where we take 600 km s^{-1} that is valid for $r > 0.7$ kpc (Figure 4). In general, we find the ionized outflow in M 82 studied in emission-line matches the scaling relationships derived from the CLASSY sample based on absorption-line data.

Similarly, in Figure 6, we compare the integrated (total) mass, momentum, and energy outflow rates with the mass, momentum, and energy input (i.e., SFR, \dot{P}_{\star} , \dot{E}_{\star}) provided by the starburst regions, respectively (Xu et al. 2022). For M

Table 1. Comparisons of Spatially Resolved Outflow Rates from Different Phases in M 82^(*)

Phases	Tracer	Log(V_{out}) ^(a) (km/s)	Log(\dot{M}_{out}) (M_{\odot}/yr)	Log(\dot{P}_{out}) (dynes)	Log(\dot{E}_{out}) (ergs/s)	Radii ^(b) (kpc)	Reference
Warm ionized	H α	2.8	0.8 – 0.0	34.3 – 33.9	41.7 – 41.4	0.7 – 2.2	This paper
Cold atomic	H I 21cm	2.3	0.5 – 0.1	33.6 – 33.2	40.6 – 40.2	1.0 – 2.2	Martini et al. (2018)
Cold molecular	CO	2.2	1.0 – 0.3	34.0 – 33.3	40.9 – 40.2	1.0 – 2.2	Leroy et al. (2015)

Note. –

(*) For the cold atomic and molecular gas, we assume that the deprojection factor is the same as applied to the warm ionized gas (DF = 2, see Shopbell & Bland-Hawthorn 1998; and Section 3.3).

(a). These outflow velocities are used with the mass outflow rates to compute \dot{P}_{out} and \dot{E}_{out} . For H α , we adopt the V_{out} from Shopbell & Bland-Hawthorn (1998).

(b). The values for all parameters cover the corresponding range in radii shown in this column.

(c). The relevant values for the M 82 starburst are Log(SFR) = 0.9 (M_{\odot}/yr), Log(\dot{P}_{\star}) = 34.6 (dynes), and Log(\dot{E}_{\star}) = 42.5 (ergs/s).

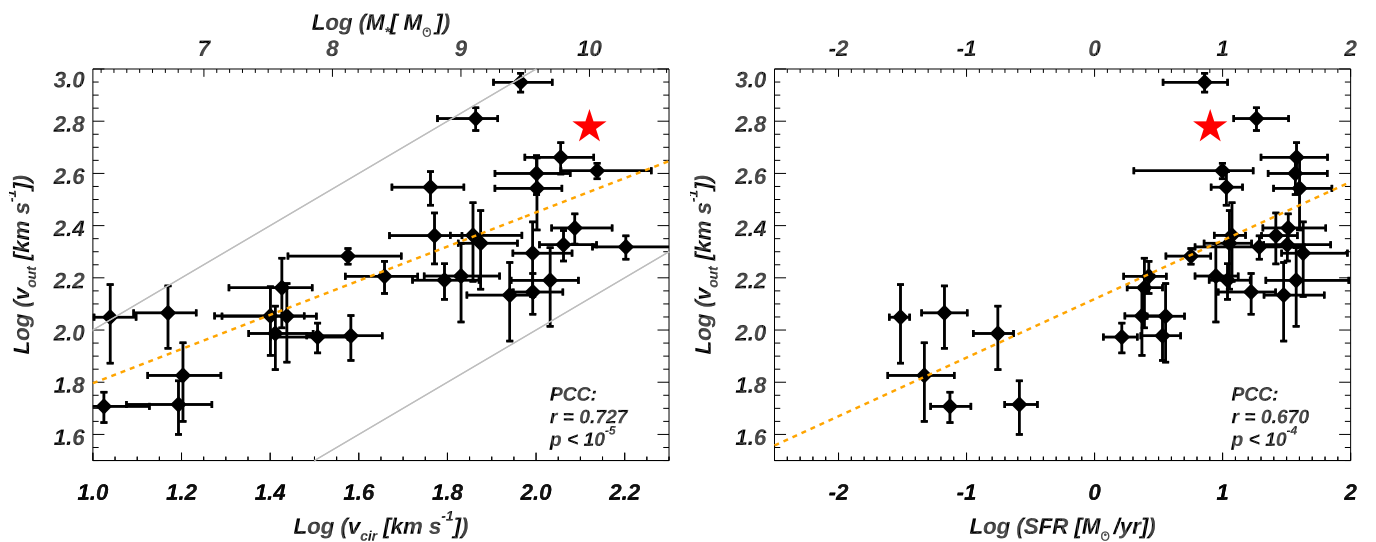


Figure 5. The log of the outflow velocity (V_{out}) versus circular velocity (**Left**) and star formation rate (**Right**). Galaxies from the CLASSY sample is shown in black, while measurements for in M 82 in this paper are shown as the red star. Orange dashed lines represent the best-fit linear correlation presented in Xu et al. (2022). In general, the galactic winds in M 82 match the scaling relationships reported for low-redshift SF galaxies in CLASSY.

82, we show the mean values for radii between 0.5 and 2.2 kpc. We find these outflow rates in M 82 well match the trends reported for the CLASSY sample. In the top panels, we also show the mass-loading factor ($\dot{M}_{\text{out}}/\text{SFR}$) versus V_{out} and V_{cir} , where M 82 is located at the bottom-right corner. Again, the location of M 82 in these plots is consistent with the CLASSY sample.

Furthermore, the median value of FF for CLASSY galaxies is 4×10^{-3} . This is similar to the one for M 82 ($\sim 10^{-3}$ to 10^{-4} , Figure 4). Given the best-fit $n_e(r)$ and FF(r) in Figures 2 and 4, we find $\text{FF} \times n \propto r^{-3}$. Then we can also derive the LOS integrated outflow column density from H α +[S II] observations as:

$$N_{\text{H,LOS}}(r) = \int_{500\text{pc}}^{\infty} \text{FF} \times n \times dr = 3.2 \times 10^{20} \text{ cm}^{-2} \quad (5)$$

This value is quite close to the median $N_{\text{H,LOS}} = 4.9 \times 10^{20} \text{ cm}^{-2}$ measured in the CLASSY sample.

Overall, we find that the warm ionized outflows probed by H α emission lines in M 82 follow the same scaling relationships and have similar LOS column densities as those reported in the CLASSY sample (Xu et al. 2022; 2023) for warm ionized outflows studied in absorption. This suggests that the outflow properties in M 82 are similar to those in other low-redshift starburst galaxies, and that the ionized gas seen in emission and absorption is likely to trace similar material. We summarize all these comparisons in Table 2³.

4.3. Constraints on Outflow Cloud Parameters

³ We refer readers to Table 3 in Xu et al. (2022) for more comparisons between CLASSY and other low-redshift starburst galaxy samples.

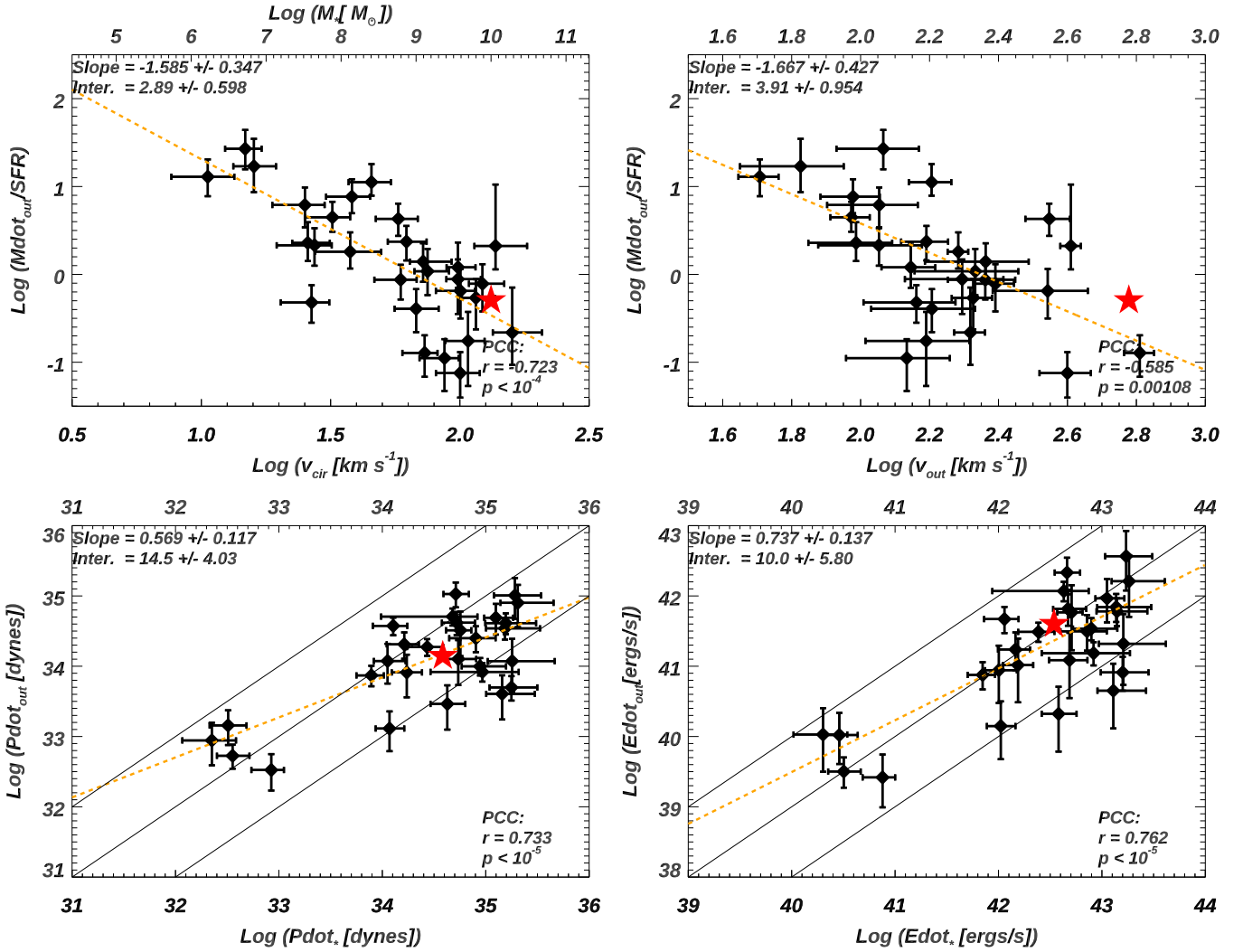


Figure 6. Top: Correlations related to the mass loading factor ($\dot{M}_{\text{out}}/\text{SFR}$). Labels and captions are the same as Figure 5. **Bottom:** Correlations of the momentum (energy) outflow rates versus momentum (energy) supplied by the starburst. See discussion in Section 4.2.

Outflows are in the form of separate clouds, whose sizes (R_{cl}), masses (M_{cl}), and column densities ($N_{\text{H,cl}}$) are key parameters to determine whether they can survive long enough to be accelerated by the hot wind (e.g., Gronke & Oh 2020; Li et al. 2020; Sparre et al. 2020; Kanjilal et al. 2021; Abruzzo et al. 2022; Fielding & Bryan 2022). Thus, these parameters are critical to decipher if outflows can still be significant at large scales within a galaxy. Nonetheless, observational constraints of them are rare in the literature (except in Xu et al. 2023).

As shown in Xu et al. (2023), one can estimate R_{cl} and $N_{\text{H,cl}}$ as follows [see their Section 4.4]:

$$R_{\text{cl}}(r) = \frac{3}{4} \frac{\text{FF}}{\text{CF}_{sh}} L(r) \quad (6)$$

$$N_{\text{H,cl}}(r) = R_{\text{cl}}(r) \times n_{\text{H,cl}}(r)$$

where $L(r)$ is the line-of-sight (LOS) path-length through the outflow, $\text{CF}_{sh} = \text{CF}/\beta_{sh}$ is the outflow LOS covering factor

after accounting for shadowing effects. This is because the projected areas by different outflow clouds within the LOS can overlap so that the total covered area drops by a factor of β_{sh} .

In M82, we do not have direct estimates of CF_{sh} . Given the similarities of outflows seen in M82 and CLASSY galaxies (see Section 4.2), we adopt the median value of CF_{sh} from CLASSY sample as a rough estimate (~ 1.7). Overall, from radius of 0.5 to 2 kpc, we get $R_{\text{cl}} = 0.9 - 0.07$ pc and $N_{\text{H,cl}} = 10^{20.7} - 10^{19.1} \text{cm}^{-2}$. We also show the distributions for them in Figure 7.

We can compare the above derived warm-ionized outflow cloud properties to the results in Krieger et al. (2021), which attempted to constrain the molecular cloud properties in M 82 based on CO(1-0) observations. They find the molecular clouds are much larger (50 ± 10 pc) and slower moving than the ionized clouds. Comparing with galaxies in CLASSY

Table 2. Comparisons of Outflows in M 82 and CLASSY^(*)

Parameters (1)	Unit (2)	M 82 (3)	CLASSY (4)
$\text{Log}(\dot{M}_{\text{out}}/\text{SFR})$	(1)	-0.30	-0.60
$\text{Log}(V_{\text{out}}/V_{\text{cir}})$	(1)	0.60	0.55
$\text{Log}(\dot{P}_{\text{out}})$	(dynes)	34.1	34.2
$\text{Log}(\dot{E}_{\text{out}})$	(ergs s ⁻¹)	41.6	41.3
$\text{Log}(N_{\text{H,LOS}})^{(a)}$	(cm ⁻²)	20.5	20.7
$\text{Log}(n_e)$	(cm ⁻³)	1.7 to 2.3	1.5
$\text{Log}(\text{FF})$	(1)	-2.6 to -4.1	-2.5
$\text{Log}(R_{\text{cl}})^{(b,c)}$	(pc)	-1.2 to -0.0	0.7
$\text{Log}(N_{\text{H,cl}})^{(b,c)}$	(cm ⁻²)	19.1 to 20.7	20.8

Note. –

(*). For M 82 values related to outflow rates (first four rows), we show the mean values between radii of 0.5 and 2.2 kpc. For M 82's outflow cloud properties (latter four rows), we present the values correspond to the range in radii of 0.5 – 2.2 kpc. For CLASSY sample, we list their published median values (Xu et al. 2022; 2023). See discussion in Section 4.2.

(a). The line-of-sight integrated hydrogen column density (see Equation 5).

(b). The cloud properties for M 82 are derived in Section 4.3.

(c). The cloud radii and column densities for M 82 assume that the cloud covering factor has the median value derived for the CLASSY sample (see equation 6).

sample, our measured R_{cl} and $N_{\text{H,cl}}$ values are also 0.2 – 2 dex smaller (see the last two rows in Table 2).

4.4. Comparisons with Theory

4.4.1. Description of Models and Simulations

The results we have presented can be compared to recent models and simulations of outflows that are designed to capture the physical processes occurring in the multi-phase galactic winds. Here we focus on two recent investigations of multi-phase galactic winds, namely the semi-analytic models by Fielding & Bryan (2022) and the high-resolution numerical simulations by Schneider et al. (2020)⁴ In both cases, there is an important distinction between the tenuous and high-velocity "wind fluid" that is created by the thermalized ejecta (winds and supernovae) of massive stars, and the denser, slower-moving ambient gas with which it interacts ("outflowing clouds"). The reported warm ionized outflow through H α in this paper represents only the latter phase. Fielding & Bryan (2022) and Schneider et al. (2020) represent significant improvements on previous models and simulations. The Fielding & Bryan (2022) model is the first to incorporate physically-based mechanisms for the exchange

⁴ There are other recent numerical simulations of outflows (Kim et al. 2020; Steinwandel et al. 2022; Rey et al. 2023), however these simulations are very poor matches to M 82 in terms of the galaxy mass, SFR, and SFR/A.

of mass, momentum, and energy between the clouds and the wind. The Schneider et al. (2020) simulations combine significantly-improved spatial resolution that better captures the underlying physics, and more realistic treatments of how mass and energy are injected by the massive stars.

In the Fielding & Bryan (2022) semi-analytic model, the wind fluid created by stellar ejecta in the starburst interacts with a population of pre-existing clouds in which there can be a two-way exchange of mass, momentum, and energy. To match the exact conditions of M 82, we have rerun their models with $\text{SFR} = 8 M_{\odot} \text{ yr}^{-1}$, starburst radius = 300 pc, and bi-polar outflows with opening angle of 73.7 $^{\circ}$ (as derived in Section 3.2). We present the results of four settings in Figures 8 and 9 (colored lines) and compare them with our observed outflow properties from H α (black dotted lines). We discuss the comparisons in details over the next few subsections.

The simulation in Schneider et al. (2020) starts with a wind-fluid created in a super-star-clusters located inside a starburst with a radius of 1000 pc and $\text{SFR} = 20 M_{\odot} \text{ yr}^{-1}$. The starburst is embedded in a gaseous disk with a radial exponential scale-length of 1.6 kpc and a gas mass of $2.5 \times 10^9 M_{\odot}$. The spatial resolution is 5 pc. There is a temperature floor at 10⁴ K, so that the warm phase will be more homogeneous in temperature in the simulation than in reality. In the simulations the collimating effects of the disk lead to a bi-polar outflow that resembles the one in M 82.

4.4.2. Outflow Properties

We begin by comparing the radial profiles of the outflow velocity (V_{out}) and outflow rates of the warm ionized gas in M 82 to the predictions of Fielding & Bryan (2022) and Schneider et al. (2018). The former is shown in Figure 8 and the latter is summarized in Tables 3.

For models by Fielding & Bryan (2022), blue and red lines represent models that produce faster, less denser winds and slower, denser winds, respectively (hereafter, FW and SW models). The dashed and solid lines represent different initial outflow cloud masses⁵. Our measured values from H α in M 82 are shown as the black dotted lines. We find the ones with $M_{\text{cl}} = 10^1 M_{\odot}$ predict larger velocities than are observed, and the agreement is better for the most massive clouds ($M_{\text{cl}} = 10^6 M_{\odot}$). The model with a slower and denser wind fluid (red curves) predicts lower velocities (more consistent with M 82). For \dot{M}_{out} , the FW model with lower mass clouds (blue solid line in the second panel) produce \dot{M}_{out} values that do not match the data for M82: the rates are too small and decline too quickly with radius. Their SW model (red lines) shows a better match to our measurements. For \dot{E}_{out} , the FW model with lower M_{cl} and SW model with higher M_{cl}

⁵ The outflow clouds in the model by Fielding & Bryan (2022) are added gradually into the model at $r = 300 - 400$ pc

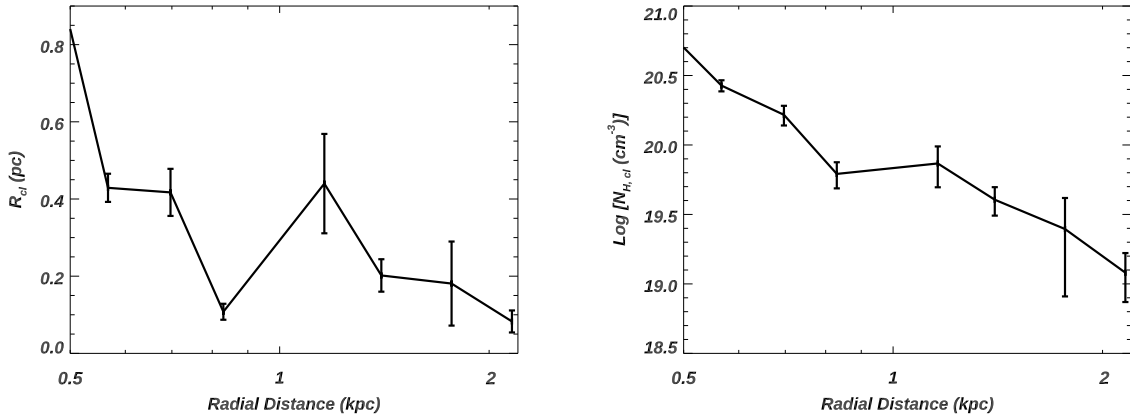


Figure 7. Left: Radial distribution of the outflow cloud sizes. **Right:** Radial distribution of the cloud hydrogen column density ($N_{H,cl}$) for the outflows. See Section 4.3 for details.

match better with the data. For \dot{P}_{out} , the SW model with initial M_{cl} between our two cases should match the data better.

On the other hand, we find that the outflow velocities are under-predicted in the Schneider et al. (2020) simulation (Tables 3). The simulation also shows a steady increase in outflow velocity with increasing radius, which is barely seen in M 82. In the columns (4) and (5) of Table 3, the values of \dot{M}_{out} derived for the warm ionized gas (normalized for the SFR) in the Schneider et al. (2020) simulation are significantly smaller than the values measured for M 82.

4.4.3. Radial Density and Pressure Profiles

Next, we compare the measured the radial density gradient in the warm ionized outflow in M 82 (Figure 2) to predictions from the two papers described above. Fielding & Bryan (2022) have shown the radial profile of the gas pressure P in the outflows. To convert our electron densities in M 82 to pressures (P), we take $P/k_B = 2n_e T$, and assume $T \sim 10^4$ K for the warm ionized gas. This is appropriate for photoionized gas (Schneider et al. 2020; Xu et al. 2022)⁶. In the left panel of Figure 9, it is clear that the predicted wind pressures by Fielding & Bryan (2022) are too low in all four models. The discrepancies grow with distance, reaching about a factor of ~ 30 to over 100 at a distance of 2 kpc.

One possible interpretation of this would be that the densities (and hence the pressures) derived from the [S II] doublet ratio are biased to higher-than-average values. This could occur if there is a range in density along a line-of-sight, and the [S II] emission is weighted towards the higher density regions (since the emissivity per unit volume is proportional to

⁶ If the emission-line gas is shock-heated, it will have a higher temperature and hence a higher inferred pressure. This will only strengthen our conclusions below.

n^2).⁷ To test this, we can compare the pressures derived from [S II] for the warm phase to those derived independently for the hot X-ray-emitting phase. This is reasonable, since there is a close morphological correspondence between the optical and soft X-ray emission in the M 82 outflow (Heckman & Thompson 2017). Therefore, in the same panel, we also overlay the radial wind pressure profile derived from X-ray measurements of M 82 in Lopez et al. (2020) (green line). Since they assume X-ray volume filling factors (FF_X) of unity and since $P_X \propto FF_X^{-1/2}$, their measurements are strict lower limits, corresponding to minimum pressures $\sim 25\%$ as large as our estimates. We emphasize that the complex filamentary structure seen in the soft X-ray emission is inconsistent with unit filling factor⁸. Even if $FF_X = 1$, all the models significantly underpredict P_X for $r > 0.7$ kpc.

Comparison with the numerical simulation in Schneider et al. (2020) shows the same discrepancy (the last three columns in Table 3). In their simulations, a bi-conical outflow naturally develops, which resembles M 82. They adopt an SFR = $20 M_\odot \text{ yr}^{-1}$, so we reduce their predicted densities by a factor $20/8 = 2.5$. In their model, the starburst extends to a radius of 1 kpc, so we only compare their predicted range in outflow density to our data at radii of 1 and 2 kpc. The predicted pressures are 30 to 70 times lower than our measurements.

We note that in both the model and simulation, the rapid radial drop in the predicted density in the warm gas is caused by the rapid drop in the thermal pressure (P_{th}) in the wind fluid (via both a r^{-2} drop in density and by the associated

⁷ If the [S II] densities are indeed biased high (by some factor $B \gg 1$, as required to match the thermal pressures in the models), then all the observed outflow rates in Figure 8 would be boosted by $B \gg 1$, and become unphysically large.

⁸ The pressures derived from the [S II] ratios and the X-ray data would agree for $FF_X \sim 0.06$.

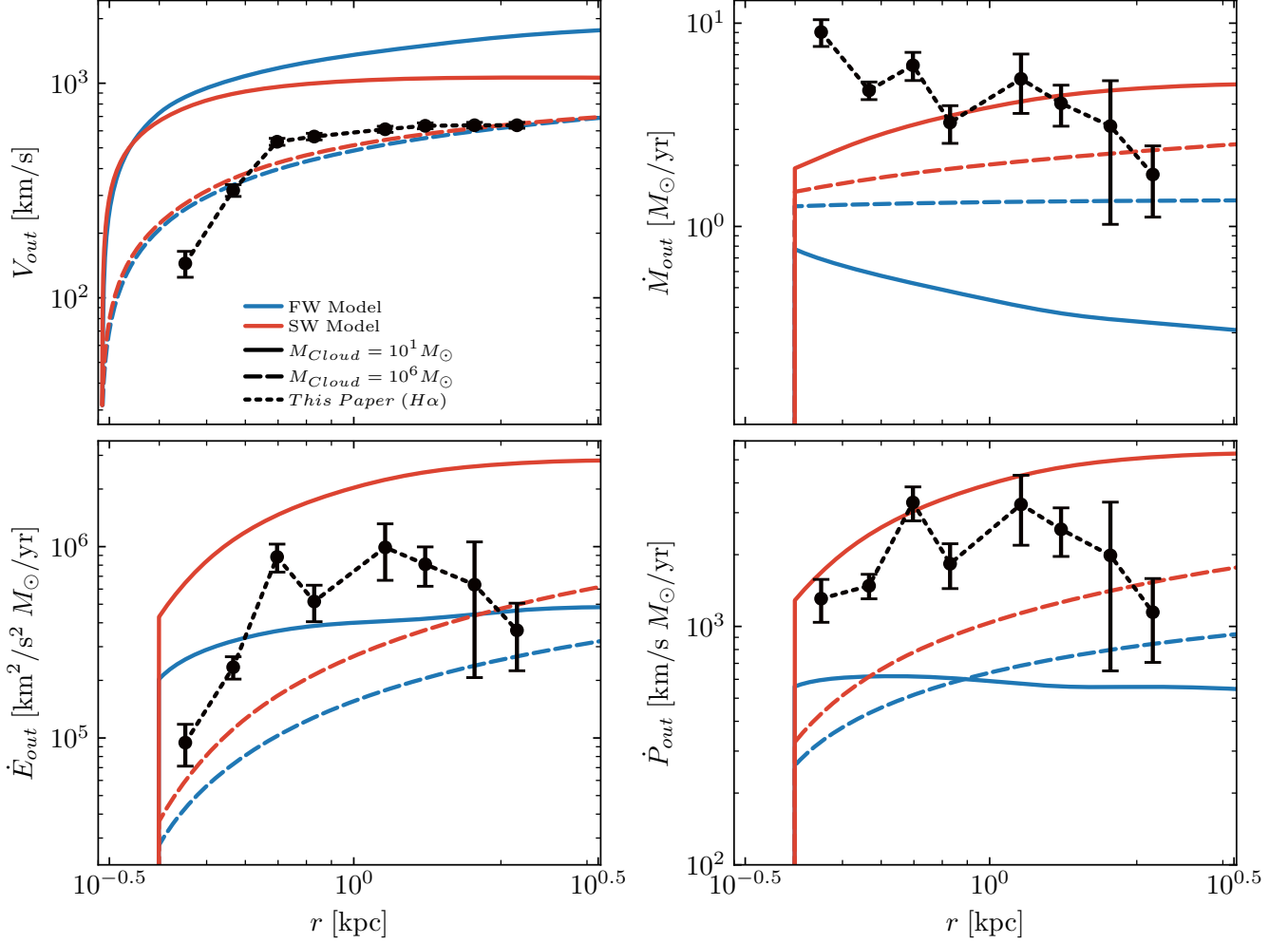


Figure 8. Comparisons of the semi-analytic models by Fielding & Bryan (2022) with the derived outflow parameters in this paper. We have rerun their models to match the input parameters of M 82 (i.e., SFR = $8 M_{\odot} \text{ yr}^{-1}$, starburst radius = 300 pc, and bi-polar outflows with opening angle of 73.7°). The blue and red lines represent the models with initial hot phase mass loading factor as 0.1 and 0.5, respectively. The former produces faster and less dense hot wind fluid (hereafter, FW model), while the latter generates slower and denser wind fluid (hereafter, SW model). The solid and dashed lines represent different outflow cloud mass into the models, i.e., 10^1 and $10^6 M_{\odot}$, respectively. In the four panels, we show the model predicted outflow cloud velocity, mass, energy, and momentum outflow rate, respectively. In each panel, we overlay our observed outflow properties from H α as black dotted lines with errorbars. We discuss these comparisons in detail in Section 4.4.

Table 3. Comparisons of Outflows Properties from M 82 and Schneider et al. (2020)^(*)

Radius (1)	$V_{\text{out, S+}}$ (2)	$V_{\text{out, M 82}}$ (3)	$(\dot{M}_{\text{out}}/\text{SFR})_{\text{S+}}$ (4)	$(\dot{M}_{\text{out}}/\text{SFR})_{\text{M 82}}$ (5)	$P_{\text{th, S+}}$ (6)	$P_{\text{ram, S+}}$ (7)	$P_{\text{M 82}}$ (8)
500	...	200	...	0.37	4.2×10^6
1000	100 to 300	600	0.02	0.25	1.0×10^5	4.6×10^5	1.8×10^6
2000	200 to 500	600	0.03	0.13	1.3×10^4	2.1×10^5	9.0×10^5

Note. –

(*). Radius is in unit of parsec, while all velocities are in units of km s^{-1} and pressures are in units of Pa/K. The mass outflow rates are normalized by the SFR.

(2), (4), (6) and (7): Model predictions from Schneider et al. (2020). For pressures, we have divided their values by 2.5 to correct for the lower SFR in M 82 compared to the model.

(5) and (8): Results derived in this paper based on rest-optical observations of M 82 (see Figure 4). The pressures in M 82 are derived from the measured n_e (see Figure 2 and Section 4.4.3).

adiabatic cooling), and by the assumption that the warm ionized clouds are in balance with P_{th} of the wind fluid. This mismatch between the models and the data implies that the clouds we observed are highly over-pressured relative to P_{th} of the wind fluid. In contrast, Heckman et al. (1990) and Lehnert & Heckman (1996) showed that the radial density profiles in starburst outflows (including M 82) could be explained if the cloud pressure is set by the ram pressure (P_{ram}) of the wind fluid. The ratio of the ram and thermal pressure in the wind fluid will be $5/3 M^2$, where M is the Mach number in the wind fluid. Since $M \gg 1$ in these supersonic winds, the pressure differences can be substantial.

To compute the ram pressure on the clouds, we need to use the relative velocity between the wind and the cloud rather than the wind velocity. Doing so, we then find that in both the Fielding & Bryan (2022) models and Schneider et al. (2020) simulations, the ram pressures on the clouds are indeed significantly larger than the thermal pressures, and in better agreement with the M 82 data (see the right panel in Figure 9 and Table 3).

We note that existing numerical simulations of wind-cloud interactions are not consistent with a balance between cloud thermal pressure and wind ram pressure. Regardless of the physical basis of the disagreement between theory and the data, this implies that both the numerical simulations and the semi-analytic model are missing some important physics. It is then unclear how this missing physics would affect the other theoretical predictions.

4.4.4. Other Cloud Properties

The results presented in Fielding & Bryan (2022) allow us to compare other key properties of their clouds to what we have estimated for M 82, namely the cloud radii and column densities (i.e., R_{cl} , and $N_{\text{H,cl}}$ derived in Section 4.3).

Fielding & Bryan (2022) do not plot the modelled R_{cl} , but these can be inferred from their M_{cl} and $N_{\text{H,cl}}$ values. At a fiducial distance of 1 kpc from the starburst the implied R_{cl} range from ~ 5 to 200 pc for $M_{\text{cl}} = 10^1$ to $10^6 M_{\odot}$, respectively. Our measured R_{cl} in M 82 (< 0.9 pc) are less than the lowest mass clouds in the models.

Then we can compare $N_{\text{H,cl}}$ between the models and the data. At a fiducial distance of 1 kpc, we find a range in the models of N_{H} from 1×10^{19} to $8 \times 10^{20} \text{ cm}^{-2}$ for the clouds with masses of 10^1 to $10^6 M_{\odot}$, respectively. Here, the observed M 82 warm ionized clouds are quite similar to the values in the models (see Figure 7).

We conclude that the cloud in the models have similar column density but are too large compared with our observed warm ionized outflows for M 82. In the future, we will apply similar models to the CLASSY sample to study this discrepancy more generally.

5. CONCLUSION

In this paper, we have reported the first estimates of the radial distributions of the gas density, outflow rates and cloud properties for the warm ionized gas in the M 82 wind based on the rest-optical data from the Subaru telescope. The main results are summarized as follows:

- We have derived the radial distribution of outflow densities based on [S II] $\lambda 6717, 6731$ emission lines. We find that the density drops from $\sim 200 \text{ cm}^{-3}$ at $r = 0.5$ kpc to $\sim 40 \text{ cm}^{-3}$ at $r = 2.2$ kpc, while the best-fit power-law is $n_e(r) = 100 \times (\frac{r}{1165 \text{ pc}})^{-1.17}$ (Figure 2 and Section 3.1).
- We calculated the radial distribution of the lateral width of the outflow based on the Subaru/FOCAS image of M 82. We find that the lateral width is $\sim 1.5 \times r$, where r is the outflow distance to the galactic center (Section 3.2). This leads to a total solid angle of 0.8π ster for the bi-conical $\text{H}\alpha$ outflow in M 82.
- Based on the derived outflow densities and widths, we then estimated the radial distributions of the volume filling factor (FF), which drops from $\sim 10^{-3}$ to 10^{-4} over the range of $r = 0.5$ to 2.2 kpc. This leads to the best-fit power-law as $\text{FF}(r) = 10^{-3} \times (\frac{r}{628 \text{ pc}})^{-1.8}$.
- We measured the mass/energy/momentum outflow rates and found that they drop quite slowly with radius, and stay almost unchanged between 0.8 and 2.2 kpc (Section 3.3). This suggests that the galactic winds in M 82 can indeed supply mass, momentum, and kinetic energy from the central regions out to at least a few kpc with minimal losses.
- We compared our derived maps of outflow rates from the warm ionized gas traced by $\text{H}\alpha$ to the ones from other outflowing phases in the literature. We found that the cold atomic gas traced by H I 21 cm emissions yields similar mass outflow rates compared with the warm ionized gas, but the latter carries substantially more momentum and kinetic energy. Additionally, comparing with the warm ionized gas, we found that the cold molecular gas traced by the CO emission line yields too larger mass outflow rates, but smaller momentum and kinetic energy outflow rates. In both cases, the differences are because the outflow velocity detected in $\text{H}\alpha$ is 3 – 4 times larger than the velocities seen in the H I 21 cm and CO emission lines. These velocities are consistent with a picture in which the atomic and molecular gas actually trace a fountain flow extending out to a few kpc (Section 4.1).
- By comparing to a large sample of local star-forming galaxies in the CLASSY sample studied using UV

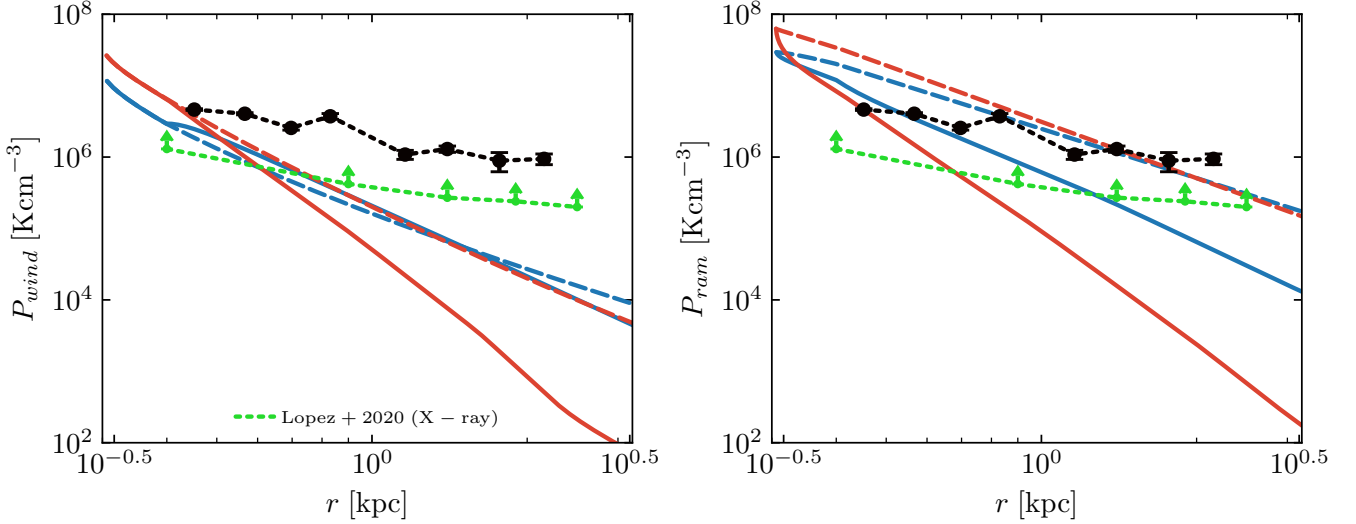


Figure 9. Same as Figure 8 but for the hot wind fluid thermal pressure (**Left**) and the ram pressure on the outflowing clouds (**Right**). In both panels, we also show the lower limits on wind pressure from the X-ray data in Lopez et al. (2020) as the green lines.

absorption-lines, we found the warm ionized outflow probed by the $H\alpha$ emission lines in M 82 follows similar scaling relationships. This suggests that the outflow properties in M 82 are similar to other local star-forming and starburst galaxies. The consistency between CLASSY and M 82 also suggests that the ionized gas seen in emission and absorption is likely to trace similar material (Section 4.2).

- We estimated the radial distributions of various outflow cloud properties, including sizes and column densities (Section 4.3). We found the the cloud sizes are typically 0.1 – 0.9 pc and cloud column densities are $10^{19.1} - 10^{20.7} \text{ cm}^{-2}$, which drops steadily from 0.5 to 2.0 kpc. These values are 0.2 – 2 dex smaller than the ones measured for the clouds in the warm ionized outflows based on the UV absorption-line data for the CLASSY sample.
- We compared the warm ionized outflows in M 82 with the theoretical models and simulations from Schneider et al. (2020) and Fielding & Bryan (2022) in Section 4.4. After accounting for geometrical and SFR differences, we found that the thermal pressures in the clouds predicted by these models are far smaller than our measured values in the M 82 data. There is better agreement with the wind ram pressures in the models and simulations.

Overall, we have presented novel measurements of radial distributions of outflow properties in M 82, includ-

ing the outflow velocity, density, rates, and cloud properties. Our work motivates similar spatially resolved studies of the ionized gas in a larger sample of galactic winds. Various essential questions await answers. For example, what are the general radial distributions of outflow properties and associated feedback? How can we adopt these radial distributions to help constrain future models and simulations of galactic winds? How are the different phases of winds connected spatially and kinetically, based on high spatial resolution, multi-wavelength data? Answering these questions will ultimately reveal the complex properties and structures of galactic winds and resolve their feedback on their host galaxies.

- 1 This research is based on data collected at the Subaru
- 2 Telescope, which is operated by the National Astronomi-
- 3 cal Observatory of Japan. We are honored and grateful for
- 4 the opportunity of observing the Universe from Maunakea,
- 5 which has the cultural, historical, and natural significance in
- 6 Hawaii.
- 7 X.X. and T.H. thank D. Fielding, G. Bryan, and M. Gronke
- 8 for useful discussions.

Facilities: Subaru Telescope

REFERENCES

Abruzzo, M. W., Fielding, D. B., & Bryan, G. L. 2022, arXiv e-prints, arXiv:2210.15679, doi: 10.48550/arXiv.2210.15679

Avery, C. R., Wuyts, S., Förster Schreiber, N. M., et al. 2022, MNRAS, 511, 4223, doi: 10.1093/mnras/stac190

- Berg, D. A., James, B. L., King, T., et al. 2022, arXiv e-prints, arXiv:2203.07357. <https://arxiv.org/abs/2203.07357>
- Bordoloi, R., Lilly, S. J., Hardmeier, E., et al. 2014, *ApJ*, 794, 130, doi: [10.1088/0004-637X/794/2/130](https://doi.org/10.1088/0004-637X/794/2/130)
- Burchett, J. N., Rubin, K. H. R., Prochaska, J. X., et al. 2021, *ApJ*, 909, 151, doi: [10.3847/1538-4357/abd4e0](https://doi.org/10.3847/1538-4357/abd4e0)
- Chevalier, R. A., & Clegg, A. W. 1985, *Nature*, 317, 44, doi: [10.1038/317044a0](https://doi.org/10.1038/317044a0)
- Chisholm, J., Tremonti, C., & Leitherer, C. 2018, *MNRAS*, 481, 1690, doi: [10.1093/mnras/sty2380](https://doi.org/10.1093/mnras/sty2380)
- Chisholm, J., Tremonti, C. A., Leitherer, C., & Chen, Y. 2017, *MNRAS*, 469, 4831, doi: [10.1093/mnras/stx1164](https://doi.org/10.1093/mnras/stx1164)
- Chisholm, J., Tremonti, C. A., Leitherer, C., Chen, Y., & Wofford, A. 2016a, *MNRAS*, 457, 3133, doi: [10.1093/mnras/stw178](https://doi.org/10.1093/mnras/stw178)
- Chisholm, J., Tremonti, C. A., Leitherer, C., et al. 2015, *ApJ*, 811, 149, doi: [10.1088/0004-637X/811/2/149](https://doi.org/10.1088/0004-637X/811/2/149)
- Chisholm, J., Tremonti Christy, A., Leitherer, C., & Chen, Y. 2016b, *MNRAS*, 463, 541, doi: [10.1093/mnras/stw1951](https://doi.org/10.1093/mnras/stw1951)
- Contursi, A., Poglitsch, A., Graciá Carpio, J., et al. 2013, *A&A*, 549, A118, doi: [10.1051/0004-6361/201219214](https://doi.org/10.1051/0004-6361/201219214)
- Davies, R. L., Förster Schreiber, N. M., Übler, H., et al. 2019, *ApJ*, 873, 122, doi: [10.3847/1538-4357/ab06f1](https://doi.org/10.3847/1538-4357/ab06f1)
- Donahue, M., & Voit, G. M. 2022, *PhR*, 973, 1, doi: [10.1016/j.physrep.2022.04.005](https://doi.org/10.1016/j.physrep.2022.04.005)
- Draine, B. T. 2011, *Physics of the Interstellar and Intergalactic Medium*
- Fielding, D. B., & Bryan, G. L. 2022, *ApJ*, 924, 82, doi: [10.3847/1538-4357/ac2f41](https://doi.org/10.3847/1538-4357/ac2f41)
- Freeman, W. R., Siana, B., Kriek, M., et al. 2019, *ApJ*, 873, 102, doi: [10.3847/1538-4357/ab0655](https://doi.org/10.3847/1538-4357/ab0655)
- Grimes, J. P., Heckman, T., Aloisi, A., et al. 2009, *ApJS*, 181, 272, doi: [10.1088/0067-0049/181/1/272](https://doi.org/10.1088/0067-0049/181/1/272)
- Gronke, M., & Oh, S. P. 2020, *MNRAS*, 492, 1970, doi: [10.1093/mnras/stz3332](https://doi.org/10.1093/mnras/stz3332)
- Heckman, T. M., Alexandroff, R. M., Borthakur, S., Overzier, R., & Leitherer, C. 2015, *ApJ*, 809, 147, doi: [10.1088/0004-637X/809/2/147](https://doi.org/10.1088/0004-637X/809/2/147)
- Heckman, T. M., Armus, L., & Miley, G. K. 1990, *ApJS*, 74, 833, doi: [10.1086/191522](https://doi.org/10.1086/191522)
- Heckman, T. M., & Best, P. N. 2023, arXiv e-prints, arXiv:2301.11960, doi: [10.48550/arXiv.2301.11960](https://doi.org/10.48550/arXiv.2301.11960)
- Heckman, T. M., & Borthakur, S. 2016, *ApJ*, 822, 9, doi: [10.3847/0004-637X/822/1/9](https://doi.org/10.3847/0004-637X/822/1/9)
- Heckman, T. M., Lehnert, M. D., Strickland, D. K., & Armus, L. 2000, *ApJS*, 129, 493, doi: [10.1086/313421](https://doi.org/10.1086/313421)
- Heckman, T. M., & Thompson, T. A. 2017, arXiv e-prints, arXiv:1701.09062. <https://arxiv.org/abs/1701.09062>
- James, B. L., Berg, D. A., King, T., et al. 2022, *ApJ*
- Kaifu, N., Usuda, T., Hayashi, S. S., et al. 2000, *PASJ*, 52, 1, doi: [10.1093/pasj/52.1.1](https://doi.org/10.1093/pasj/52.1.1)
- Kanjilal, V., Dutta, A., & Sharma, P. 2021, *MNRAS*, 501, 1143, doi: [10.1093/mnras/staa3610](https://doi.org/10.1093/mnras/staa3610)
- Kashikawa, N., Aoki, K., Asai, R., et al. 2002, *PASJ*, 54, 819, doi: [10.1093/pasj/54.6.819](https://doi.org/10.1093/pasj/54.6.819)
- Kim, C.-G., Ostriker, E. C., Fielding, D. B., et al. 2020, *ApJL*, 903, L34, doi: [10.3847/2041-8213/abc252](https://doi.org/10.3847/2041-8213/abc252)
- Krieger, N., Walter, F., Bolatto, A. D., et al. 2021, *ApJL*, 915, L3, doi: [10.3847/2041-8213/ac01e9](https://doi.org/10.3847/2041-8213/ac01e9)
- Lehnert, M. D., & Heckman, T. M. 1996, *ApJ*, 462, 651, doi: [10.1086/177180](https://doi.org/10.1086/177180)
- Leroy, A. K., Walter, F., Martini, P., et al. 2015, *ApJ*, 814, 83, doi: [10.1088/0004-637X/814/2/83](https://doi.org/10.1088/0004-637X/814/2/83)
- Li, Z., Hopkins, P. F., Squire, J., & Hummels, C. 2020, *MNRAS*, 492, 1841, doi: [10.1093/mnras/stz3567](https://doi.org/10.1093/mnras/stz3567)
- Lopez, L. A., Mathur, S., Nguyen, D. D., Thompson, T. A., & Olivier, G. M. 2020, *ApJ*, 904, 152, doi: [10.3847/1538-4357/abc010](https://doi.org/10.3847/1538-4357/abc010)
- Marasco, A., Belfiore, F., Cresci, G., et al. 2022, arXiv e-prints, arXiv:2209.02726. <https://arxiv.org/abs/2209.02726>
- Martin, C. L. 2005, *ApJ*, 621, 227, doi: [10.1086/427277](https://doi.org/10.1086/427277)
- . 2006, *ApJ*, 647, 222, doi: [10.1086/504886](https://doi.org/10.1086/504886)
- Martin, C. L., Shapley, A. E., Coil, A. L., et al. 2012, *ApJ*, 760, 127, doi: [10.1088/0004-637X/760/2/127](https://doi.org/10.1088/0004-637X/760/2/127)
- Martini, P., Leroy, A. K., Mangum, J. G., et al. 2018, *ApJ*, 856, 61, doi: [10.3847/1538-4357/aab08e](https://doi.org/10.3847/1538-4357/aab08e)
- Naab, T., & Ostriker, J. P. 2017, *ARA&A*, 55, 59, doi: [10.1146/annurev-astro-081913-040019](https://doi.org/10.1146/annurev-astro-081913-040019)
- Newman, S. F., Shapiro Griffin, K., Genzel, R., et al. 2012a, *ApJ*, 752, 111, doi: [10.1088/0004-637X/752/2/111](https://doi.org/10.1088/0004-637X/752/2/111)
- Newman, S. F., Genzel, R., Förster-Schreiber, N. M., et al. 2012b, *ApJ*, 761, 43, doi: [10.1088/0004-637X/761/1/43](https://doi.org/10.1088/0004-637X/761/1/43)
- Ohyama, Y., Taniguchi, Y., Iye, M., et al. 2002, *PASJ*, 54, 891, doi: [10.1093/pasj/54.6.891](https://doi.org/10.1093/pasj/54.6.891)
- Osterbrock, D. E., & Ferland, G. J. 2006, *Astrophysics of gaseous nebulae and active galactic nuclei*
- Perna, M., Cresci, G., Brusa, M., et al. 2019, *A&A*, 623, A171, doi: [10.1051/0004-6361/201834193](https://doi.org/10.1051/0004-6361/201834193)
- Pettini, M., Steidel, C. C., Adelberger, K. L., Dickinson, M., & Giavalisco, M. 2000, *ApJ*, 528, 96, doi: [10.1086/308176](https://doi.org/10.1086/308176)
- R Core Team. 2021, *R: A Language and Environment for Statistical Computing*, R Foundation for Statistical Computing, Vienna, Austria. <https://www.R-project.org/>
- Rey, M. P., Katz, H. B., Cameron, A. J., Devriendt, J., & Slyz, A. 2023, arXiv e-prints, arXiv:2302.08521, doi: [10.48550/arXiv.2302.08521](https://doi.org/10.48550/arXiv.2302.08521)
- Rubin, K. H. R., Prochaska, J. X., Koo, D. C., et al. 2014, *ApJ*, 794, 156, doi: [10.1088/0004-637X/794/2/156](https://doi.org/10.1088/0004-637X/794/2/156)
- Rubin, K. H. R., Weiner, B. J., Koo, D. C., et al. 2010, *ApJ*, 719, 1503, doi: [10.1088/0004-637X/719/2/1503](https://doi.org/10.1088/0004-637X/719/2/1503)

- Rupke, D. S., Veilleux, S., & Sanders, D. B. 2002, *ApJ*, 570, 588, doi: [10.1086/339789](https://doi.org/10.1086/339789)
- . 2005, *ApJS*, 160, 87, doi: [10.1086/432886](https://doi.org/10.1086/432886)
- Rupke, D. S. N., & Veilleux, S. 2013, *ApJ*, 768, 75, doi: [10.1088/0004-637X/768/1/75](https://doi.org/10.1088/0004-637X/768/1/75)
- Rupke, D. S. N., Coil, A., Geach, J. E., et al. 2019, *Nature*, 574, 643, doi: [10.1038/s41586-019-1686-1](https://doi.org/10.1038/s41586-019-1686-1)
- Sakai, S., & Madore, B. F. 1999, *ApJ*, 526, 599, doi: [10.1086/308032](https://doi.org/10.1086/308032)
- Schneider, E. E., Ostriker, E. C., Robertson, B. E., & Thompson, T. A. 2020, *ApJ*, 895, 43, doi: [10.3847/1538-4357/ab8ae8](https://doi.org/10.3847/1538-4357/ab8ae8)
- Schneider, E. E., Robertson, B. E., & Thompson, T. A. 2018, *ApJ*, 862, 56, doi: [10.3847/1538-4357/aacce1](https://doi.org/10.3847/1538-4357/aacce1)
- Shopbell, P. L., & Bland-Hawthorn, J. 1998, *ApJ*, 493, 129, doi: [10.1086/305108](https://doi.org/10.1086/305108)
- Silk, J., & Rees, M. J. 1998, *A&A*, 331, L1, doi: [10.48550/arXiv.astro-ph/9801013](https://doi.org/10.48550/arXiv.astro-ph/9801013)
- Sparre, M., Pfrommer, C., & Ehlert, K. 2020, *MNRAS*, 499, 4261, doi: [10.1093/mnras/staa3177](https://doi.org/10.1093/mnras/staa3177)
- Steidel, C. C., Erb, D. K., Shapley, A. E., et al. 2010, *ApJ*, 717, 289, doi: [10.1088/0004-637X/717/1/289](https://doi.org/10.1088/0004-637X/717/1/289)
- Steinwandel, U. P., Kim, C.-G., Bryan, G. L., et al. 2022, arXiv e-prints, arXiv:2212.03898, doi: [10.48550/arXiv.2212.03898](https://doi.org/10.48550/arXiv.2212.03898)
- Strickland, D. K., & Heckman, T. M. 2007, *ApJ*, 658, 258, doi: [10.1086/511174](https://doi.org/10.1086/511174)
- . 2009, *ApJ*, 697, 2030, doi: [10.1088/0004-637X/697/2/2030](https://doi.org/10.1088/0004-637X/697/2/2030)
- Sugahara, Y., Ouchi, M., Lin, L., et al. 2017, *ApJ*, 850, 51, doi: [10.3847/1538-4357/aa956d](https://doi.org/10.3847/1538-4357/aa956d)
- Swinbank, A. M., Harrison, C. M., Tiley, A. L., et al. 2019, *MNRAS*, 487, 381, doi: [10.1093/mnras/stz1275](https://doi.org/10.1093/mnras/stz1275)
- Veilleux, S., Maiolino, R., Bolatto, A. D., & Aalto, S. 2020, *A&A Rv*, 28, 2, doi: [10.1007/s00159-019-0121-9](https://doi.org/10.1007/s00159-019-0121-9)
- Wang, W., Kassin, S. A., Faber, S. M., et al. 2022, *ApJ*, 930, 146, doi: [10.3847/1538-4357/ac6592](https://doi.org/10.3847/1538-4357/ac6592)
- Weiner, B. J., Coil, A. L., Prochaska, J. X., et al. 2009, *ApJ*, 692, 187, doi: [10.1088/0004-637X/692/1/187](https://doi.org/10.1088/0004-637X/692/1/187)
- Westmoquette, M. S., Smith, L. J., Gallagher, J. S., & Walter, F. 2013, *MNRAS*, 428, 1743, doi: [10.1093/mnras/sts154](https://doi.org/10.1093/mnras/sts154)
- Wood, C. M., Tremonti, C. A., Calzetti, D., et al. 2015, *MNRAS*, 452, 2712, doi: [10.1093/mnras/stv1471](https://doi.org/10.1093/mnras/stv1471)
- Xu, X., Heckman, T., Henry, A., et al. 2022, *ApJ*, 933, 222, doi: [10.3847/1538-4357/ac6d56](https://doi.org/10.3847/1538-4357/ac6d56)
- . 2023, arXiv e-prints, arXiv:2301.11498, doi: [10.48550/arXiv.2301.11498](https://doi.org/10.48550/arXiv.2301.11498)
- Yoshida, M., Kawabata, K. S., Ohyama, Y., Itoh, R., & Hattori, T. 2019, *PASJ*, 71, 87, doi: [10.1093/pasj/psz069](https://doi.org/10.1093/pasj/psz069)
- Yoshida, M., Shimizu, Y., Sasaki, T., et al. 2000, in Society of Photo-Optical Instrumentation Engineers (SPIE) Conference Series, Vol. 4009, Advanced Telescope and Instrumentation Control Software, ed. H. Lewis, 240–249, doi: [10.1117/12.388394](https://doi.org/10.1117/12.388394)
- Zabl, J., Bouché, N. F., Wisotzki, L., et al. 2021, *MNRAS*, 507, 4294, doi: [10.1093/mnras/stab2165](https://doi.org/10.1093/mnras/stab2165)